ENGINEERING

Adaptive locomotion of artificial microswimmers

H.-W. Huang[1]*, F. E. Uslu[2], P. Katsamba[3]†, E. Lauga[3], M. S. Sakar[2]*, B. J. Nelson[1]‡

Bacteria can exploit mechanics to display remarkable plasticity in response to locally changing physical and chemical conditions. Compliant structures play a notable role in their taxis behavior, specifically for navigation inside complex and structured environments. Bioinspired mechanisms with rationally designed architectures capable of large, non-linear deformation present opportunities for introducing autonomy into engineered small-scale devices. This work analyzes the effect of hydrodynamic forces and rheology of local surroundings on swimming at low Reynolds number, identifies the challenges and benefits of using elastohydrodynamic coupling in locomotion, and further develops a suite of machinery for building untethered microrobots with self-regulated mobility. We demonstrate that coupling the structural and magnetic properties of artificial microswimmers with the dynamic properties of the fluid leads to adaptive locomotion in the absence of on-board sensors.

INTRODUCTION

Microorganisms manifest a diverse set of molecular motility machinery to effectively navigate complex environments and occupy a variety of ecological niches (1). Swimming in bacteria arises from the mechanical interactions between the actuated flagella, cell body, and the drag generated by the flow (2, 3). Hydrodynamic drag is dominated by viscous forces at low Reynolds number, which, in turn, depend on the shape of the moving object. Bacteria can adopt alternate shapes and sizes over the course of their life cycles to optimize their motility (4–6). In addition to modulating cell body shape, bacteria can also use the form and structure of the propulsive system for advanced maneuverability in complex environments. Bending of the hook enhances motility in *Caulobacter crescentus* (7), while monotrichous *Vibrio alginolyticus* outperforms multiflagellated *Escherichia coli* in climbing nutrient gradients with the aid of a flagellar buckling instability (8). A polymorphic transition in the flagellar filament enables *Shewanella putrefaciens* to escape from physical traps (9).

The development of microscopic artificial swimmers that can cross biological barriers, move through bodily fluids, and access remote path-ological sites can revolutionize targeted therapies (10–13). Seminal work demonstrated the feasibility of following the example of prokaryotic (14, 15) or eukaryotic (16) flagellum for building magnetically controlled microswimmers that have the ability to exhibit nonreciprocal motion. However, unlike living cells, these mechanical devices neither sense their local environment nor react to changes in physical conditions. Addressing these issues with traditional robotic solutions based on electronic circuitry would require highly sophisticated manufacturing processes and result in orders of magnitude increase in the size of the machines. Utilization of biological actuators and sensors for engineering autonomous biohybrid robotic devices is an intriguing alternative (17). Although the field is in its infancy, proof-of-concept examples have already demonstrated the potential (18–20). Here, we focus on artificial materials to pave the way for building robust, tunable, and durable engineering solutions.

Fluid-structure coupling in hydrogel-based compliant machinery may present a possible mechanism for autonomous regulation of morphology and function. Using origami design principles as a framework, a variety of folding techniques have been introduced for the development of three-dimensional (3D) flexible microstructures (21). Production of programmable self-folding films at microscale can be achieved via patterning of multiple layers with different swelling properties (22–24) or creation of spatial concentration gradients (25, 26). However, these methods provide limited control over the mechanical and magnetic properties of the machine. In our previous work, we have shown that the form and magnetization profile of self-folded micromachines can be independently programmed by incorporating magnetic nanoparticles (MNPs) into sequentially patterned hydrogel layers (27). In this work, we introduce a simple and versatile method for engineering magnetically controlled soft micromachines as 3D reconfigurable multibody systems from a nanocomposite hydrogel monolayer. We present a set of design strategies for self-regulation of motility and maneuverability by using the interplay among viscous, elastic, magnetic, and osmotic forces. We show that reconfigurable body can continuously morph in accordance with the properties of the surrounding fluid, a feature that leads to passing through constrictions and enhancement of locomotion performance. Using elastohydrodynamic coupling in shape-shifting and gait adaptation enables enticing opportunities for microrobots navigating inside obstructed, heterogeneous, and dynamically changing environments.

RESULTS AND DISCUSSION

Building soft microswimmers with bioinspired locomotion

We followed a variant of origami, called kirigami, to design and fold compliant 3D microstructures from a thermoresponsive gel composite reinforced with MNPs. The fabrication process involves cutting initiated by photolithography and folding upon hydration of the polymerized layer. We generated nonuniform distribution of MNPs along the thickness direction to form two distinct layers of hydrogels with significantly different swelling ratios through sedimentation or application of magnetic forces. Differential swelling upon hydration along the film thickness resulted in self-folding of monolayer structures (see section S1). The curvature of the folded sheet was proportional to the MNP concentration (fig. S1). The folding axis of each compartment was parallel to the alignment of encapsulated MNPs due to constrained swelling in the direction of reinforcement. Particle alignment was performed by the application of uniform magnetic fields during sample preparation (fig. S2). The folding axis and the magnetic anisotropy of each compartment were coupled to each other and both defined by the orientation of the

[1]Department of Mechanical Engineering, ETH Zurich, CH-8092 Zurich, Switzerland. [2]Institute of Mechanical Engineering, Ecole Polytechnique Fédérale de Lausanne, CH-1015 Lausanne, Switzerland. [3]Department of Applied Mathematics and Theoretical Physics, University of Cambridge, Cambridge CB3 0WA, UK.
*These authors contributed equally to this work.
†Present address: School of Mathematics, University of Birmingham, Edgbaston, Birmingham B15 2TT, UK.
‡Corresponding author. Email: bnelson@ethz.ch

reinforcing MNPs. We fabricated hundreds of micromachines with complex 3D architectures from the same film using a single-step photolithography process (Fig. 1A).

We focused on three different configurations inspired by widely studied microorganisms, *C. crescentus*, *Helicobacter pylori*, and *Borrelia burgdorferi* (Fig. 1B). Bacteria swim by rotating propeller-like organelles, called flagellar filaments, which extend from the cell body (28). Artificial microswimmers can mimic this motion if the magnetic moment of the machine is perpendicular to its long axis (29). We explored the effect of shape anisotropy on the magnetization profile of the microswimmers. In-plane (*x-y* plane) alignment of MNPs in the unfolded monolayer resulted in a magnetization parallel to the folding axis and a misalignment angle (ϕ), which is the angle between the folding axis and magnetic fields, of zero. In other words, the structures resemble compass needles that align their long axis to the direction of the external magnetic field (30). To address this limitation, we fabricated microswimmers with varying out-of-plane particle alignment while keeping the in-plane particle alignment constant. Out-of-plane alignment of MNPs has no effect on the final 3D shape due to the relatively small thickness (~30 μm) of the monolayer compared to its overall size. With the magnetization component in *z* axis, folded structures acquired a magnetic moment in the radial direction, where ϕ was equal to the angle of the out-of-plane alignment of MNPs with respect to the *x-y* plane (Fig. 1C).

Optimal motility at different viscosities requires different gaits

Previous work on *C. crescentus* has shown that the flexibility of the hook generates cell body precession that leads to a 3D helical motion (7). The slantwise motion of the cell body during precession develops thrust, adding to that developed by the flagellar filament. On the other hand, the helical shape of *Vibrio cholerae* enhances motility within a polymer network, a feature suggested to be important for its pathogenicity (31).

We systematically explored the potential advantage of this morphological diversity by building microswimmers with different body plans and actuating them in fluids with varying viscosity. Although we did not design a separate flexible hook that connects the tail and the body, we can still engineer microswimmers that follow 3D helical trajectories by coordinating their morphology with magnetization profile (32). The Reynolds number is ranging from 10^{-2} to 10^{-4} in all the experiments presented in this work; thus, swimming is performed under laminar flow. The normalized velocity of microswimmers is reported to provide a more accurate comparison of performance (16). For this reason, we express motility as $U/fL \times 1000$, where U is the forward velocity, f is the rotating frequency, and L is the body length of the micromachines (33).

In a sucrose solution with a similar viscosity to blood (3 mPa·s), the flagellated microswimmers with a tubular body and a flexible planar tail moved much faster compared to other prototypes (Fig. 1D). The superior performance of this configuration compared to tubular body–helical tail and helical body–helical tail combinations can be explained by the enhanced body precession induced by the oar-like propulsion of the tail. Misalignment of the body with respect to the external magnetic field, together with the flexibility of the tail, leads to helical motion. The forward motility of the flagellated microswimmers was significantly higher when $\phi = 30°$ (Fig. 1E). While flagellated microswimmers benefited from both helical motion and corkscrew motion in this configuration, helical microswimmers suffered from extra drag generated by wobbling. Tuning ϕ to 90° resulted in a completely different picture. The motility of the flagellated swimmers markedly dropped because of the absence of helical motion, while helical microswimmers performed corkscrew motion without wobbling. These results show that the presence of a nonhelical body is advantageous if the body can generate large-amplitude helical motion.

The increase of viscosity monotonically decreased the motility of all microswimmers, but the drop was drastic for flagellated microswimmers
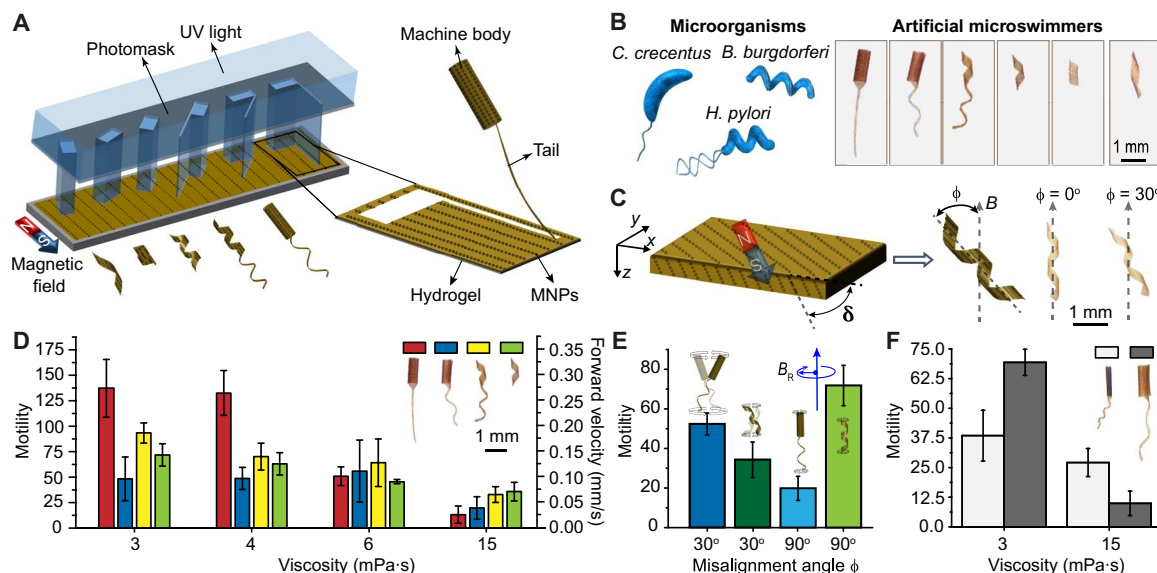
Fig. 1. Design, development, and actuation of bioinspired microswimmers. (**A**) A kirigami approach to building mass customized soft microswimmers through a single-step photolithography. UV, ultraviolet. (**B**) Schematic illustration of the bacteria taken as inspiration for this study and the optical images of the engineered artificial microswimmers. (**C**) Out-of-plane alignment ($\delta \neq 0$) of MNPs lead to nonzero misalignment angle ϕ. The optical images showing two swimmers with identical shapes and varying ϕ are shown. (**D**) A comparison of the motility of microswimmers swimming in fluids with different viscosities. (**E**) Motility of the flagellated tubular microswimmers and helical microswimmers encoded with two different magnetic anisotropies rotating in a solution with a viscosity of 3 mPa·s. (**F**) Effect of body size on the motility of the tubular microswimmers. The swimmers were driven at 2 Hz with a field strength of 20 mT in all experiments, unless stated otherwise. All bar graphs represent average ± SEM (n = 6 measurements for each microswimmer and three different swimmers tested per condition).

with a planar tail. With increasing viscosity, viscous forces start to attenuate helical motion of the cell body, and the body becomes a source of passive drag that primarily impedes the motility. Furthermore, the lack of wobbling on the body eliminates bending of the tail, and in the absence of chirality, the tail cannot break the time-reversal symmetry to generate propulsion. Helical microswimmers were the fastest at high viscosity because the only relevant motion became the corkscrew motion. The body of microswimmers had a higher magnetic torque compared to their tail, and thrust was mainly generated by the body, which made the tail obsolete at high viscosity. A larger body provided higher motility at low viscosity because those machines traced a helical path of higher amplitude (see section S2 and fig. S3). However, at high viscosity, body precession was attenuated, and therefore, smaller body provided higher motility (Fig. 1F). Our results conflict with the argument that helical body does not provide a significant enhancement of motility for *H. pylori* inside viscous solutions (*34*). The reason for this discrepancy lies in the body rotation; only the flagellum is actively rotated in bacteria, and their bodies show a very slow counterrotation to balance torque while we are simultaneously rotating the body and the tail with the same angular speed.

Morphology and magnetization profile together determine performance during navigation

Along with motility, maneuverability plays a key role for bacteria in rapidly detecting and tracking nutrient gradients. By adjusting the relative frequency and the length of reorientation phases, cells are able to adapt to the changing local chemical environment. Experimental evolutionary analysis of motile behavior of *E. coli* has shown that evolved strains had increased swimming velocity and frequency of reorientation, which together led to enhanced chemotaxis in porous media (*35*). Experiments with *E. coli* have also shown that body size and shape control the average reorientation angle and time for a motile cell to change its direction of motion (*36*). We investigated the maneuverability of artificial microswimmers by inducing deflections in the yaw angle during swimming (Fig. 2). A highly maneuverable microswimmer is expected to quickly change its movement direction with a small change in control signal. For gentle disturbances where the orientation of the rotating magnetic field is instantaneously changed for less than 10° around the yaw axis, all swimmers corrected their heading almost immediately. For stronger perturbations with 45° yaw rotation, both the body and tail geometry played an important role in the dynamic response of the compliant swimmers.

During a successful maneuver, the body responds to the control signal before the tail, as the magnetization of the body is significantly higher. The speed of body rotation in response to the applied torque depends on the magnetization of the body and the hydrodynamic drag, which, in turn, are determined by the body geometry and magnetic volume. The rapid change in body orientation generated a buckling instability on the flexible tail for swimmers with a tubular body. This instability led to a transient wobbling motion on the machine body until the tail reoriented with the main axis of the body, and this delay is quantified by the recovery time Δt_{rec} (Fig. 2A). The overall delay between the change in the control signal and the completion of reorientation of the swimming direction is denoted by Δt_{orient}. Swimmers with a planar tail are more susceptible to instabilities. The contribution of the helical tail to stabilization can be explained by the effectively higher stiffness of helical geometry compared to a planar structure and the attenuated precession on the body. At extreme cases (ϕ close to 0), change in direction resulted in a tumbling motion, which manifests itself as loss of motility (Fig. 2B). Although inertial forces play no role at a small scale, elastic instabilities occur due to the extreme compliance of the propulsion apparatus. One of the best demonstrations in nature is the flicks in *V. alginolyticus*, which arise from an off-axis deformation of the flagellum caused by the buckling of the hook (*37*). Switching the body morphology from a tube to a helix resulted in superior performance. The helical body generates propulsion together with the helical tail while applying pulling force on the filament, thus preventing buckling instability. As a result, the body and the tail simultaneously reorient along the direction of magnetic field during maneuvers (Fig. 2C). While Δt_{rec} is more than 4 s for swimmers with a tubular body, it is less than 0.5 s for swimmers with a helical body moving at the same velocity. Helical
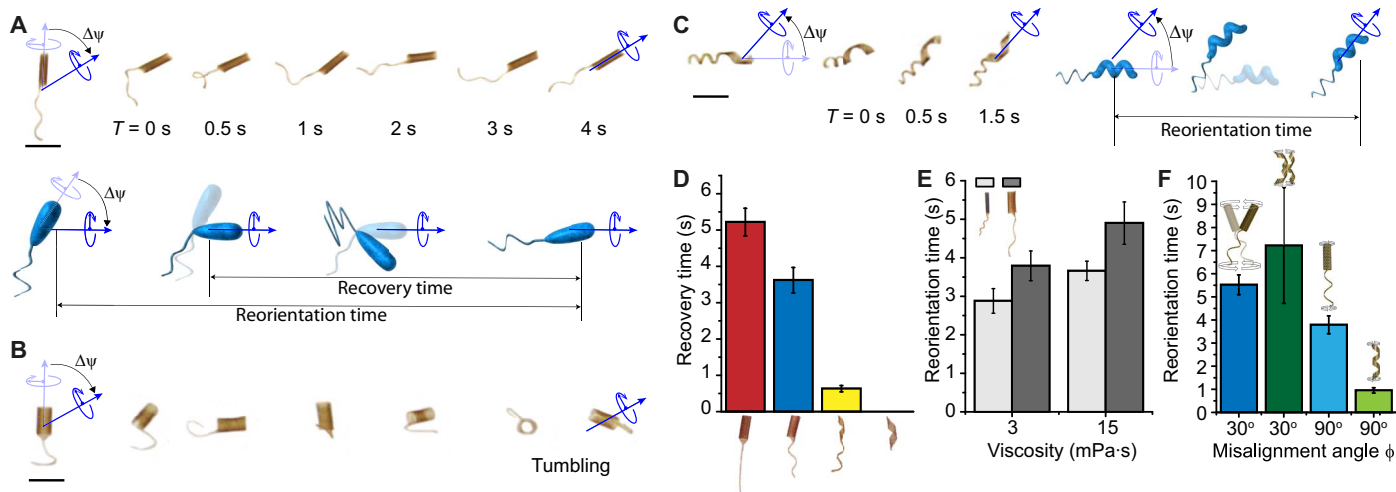
Fig. 2. Elastic instabilities and optimization of maneuverability. The yaw angle Ψ was instantly changed 45°, while the swimmers were driven at 2 Hz with a field strength of 20 mT in a solution with a viscosity of 3 mPa·s. (**A**) Time-lapse images of a microswimmer with a tubular body and helical tail during the reorientation of its swimming direction. (**B**) Changing the tail to a planar geometry and ϕ to 30° led to a complete loss of motility. (**C**) Changing the body geometry to a helix significantly reduces the reorientation time by providing instant recovery. (**D**) Quantitative comparison of reorientation time for different prototypes. (**E**) Effect of body size on the maneuverability of microswimmers swimming at varying viscosities. (**F**) Role of magnetic anisotropy on the maneuverability of the microswimmers with tubular and helical bodies. Scale bars, 1 mm. All bar graphs represent average ± SEM ($n = 6$ measurements for each microswimmer and three different swimmers tested per condition).

microswimmers showed the best performance as expected because they do not deal with body and tail coordination (Fig. 2D and movie S1). We then explored the combined effect of body size and viscosity on maneuverability using the swimmers shown in Fig. 1F. We prepared tubular machines with smaller folding diameter by increasing the nanoparticle concentration in the film formulation. Regardless of the value of the viscosity, smaller body provided a comparative advantage by lowering rotational drag and increasing magnetic torque (Fig. 2E; see section S2 for additional information).

We next studied how magnetization profile may affect maneuverability of microswimmers. So far, they were encoded with $\phi = 90°$ to prevent wobbling motion during forward swimming. Experiments on helical swimmers encoded with $\phi = 30°$ showed that wobbling motion can significantly affect Δt_{orient} during maneuvers (Fig. 2F). Likewise, Δt_{orient} of flagellated swimmers with $\phi = 30°$ was significantly higher than that of swimmers with $\phi = 90°$ because the rapid change in the yaw angle destabilized the machines and transformed the wobbling motion into a tumbling motion. To our surprise, adding a tail to the wobbling helical swimmer significantly enhanced its performance by completely preventing the occurrence of tumbling motion (movie S2). These results pose a trade-off between motility and maneuverability at low viscosity, as the reorientation time increases with decreasing ϕ and the motility increases with increasing ϕ. The capability of dynamically remagnetizing the body would provide a method for adjusting the motility and maneuverability on demand. Magnetically reinforced nanocomposites were remagnetized in a direction other than the direction of MNP alignment when the applied magnetic field was significantly higher than the magnetic field applied for the alignment of particles during fabrication (see section S3, fig. S4, and movie S3).

Exploiting elastohydrodynamic coupling for gait adaptation

Unlike swimmers with rigid propulsion mechanisms, the coupling between magnetic forces, filament flexibility, and viscous drag determines propulsion efficiency of compliant swimmers (16). This nonlinear relationship is described by dimensionless sperm number defined as

$$ \mathrm{Sp} = L_f / \left(\frac{A}{\xi_\perp \omega} \right)^{1/4} \qquad (1) $$

where L_f is the length of the flagellum and A is the bending stiffness. For a slender filament ($L_f \gg a$), the perpendicular viscous coefficient is given by $\xi_\perp = \frac{4\pi\mu_d}{\log\left(\frac{L_f}{a}\right) + 1/2}$. The radius a is approximated by the geometric mean ($a = \sqrt{t \times w}$) of the thickness t and width w of the filament. For Sp $\ll 1$, bending forces dominate, and the filament is effectively straight. Artificial microswimmers must operate away from this regime, and optimal motility is predicted for Sp of the order of unity.

We asked whether the elastohydrodynamic properties can be exploited to trigger a gait transition in response to changes in viscosity (Fig. 3A and movie S4). Analytical solution of the equations of motion for an actuated flexible tail predicted that the number of helical turns would increase with increasing Sp (see section S4 and fig. S5). The bending stiffness was obtained from the measured values of the elastic modulus of the hydrogel and the filament geometry (fig. S7). Figure 3B shows time-lapse optical images of a tubular microswimmer with a planar tail, encoded with $\phi = 30°$ swimming at different viscosities and rotating frequencies. As described before, this configuration generated a strong helical motion at low viscosity (3 mPa·s) that completely ceased
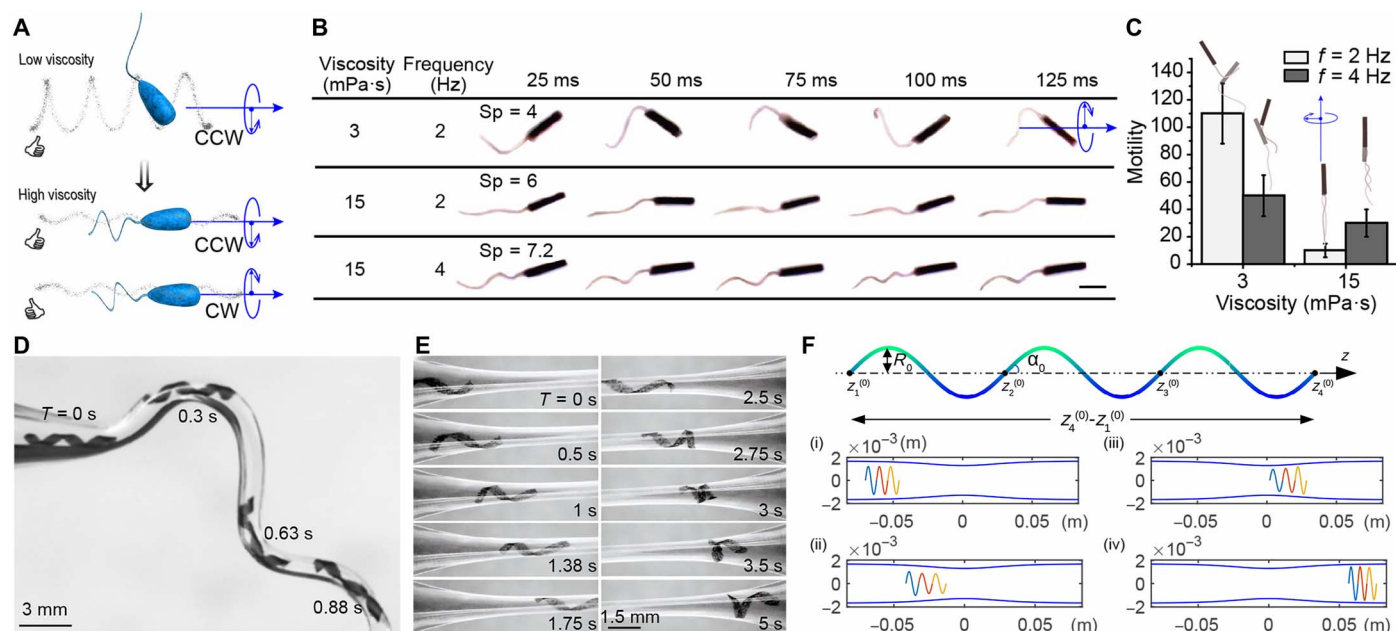
Fig. 3. The efficiency and mode of motility are controlled by the body plan. (**A**) A schematic illustration of microswimmers swimming with an oar-like propulsion strategy at low viscosity and performing corkscrew motion at high viscosity due to coiling of the flexible tail. CCW, counterclockwise; CW, clockwise. (**B**) The optical images and (**C**) motility along with schematic representations of microswimmers with shape-shifting tails moving at varying viscosities and rotating frequencies. Scale bar, 500 μm. (**D**) Optical images of a flexible helix passing through curved conduit morphologies with the flow rate of 2 ml/min. (**E**) Shape change driven by velocity gradients in a conduit with a constriction and the flow rate of 5 ml/min. (**F**) Computational model exploring shear-induced elongation in a conduit with a slowly varying constriction.

at high viscosity (15 mPa·s). At relatively low viscosity and rotation frequency (Sp = 4), the internal and external stresses were mostly dissipated at the joint, which led to body precession. Constraining the body precession by setting φ to 90° reduced motility and enabled coiling in the tail. Coiling of the tail was observable at higher viscosity and frequency (Sp = 7.2) both in the analytical solution (fig. S5) and experimental data (Fig. 3B). This morphological transformation led to the emergence of corkscrew motion and enhanced motility (Fig. 3C and fig. S5D).

Shape adaptation in complex channels under viscous flow

Gradients in ambient fluid velocity are pervasive in microbial habitats, and bacteria exhibit directed movement responses due to shear by using their body shape (38, 39). The extraordinary flexibility of red blood cells enables them to change shape under shear forces as they pass through vessels significantly smaller than their diameter (40). Inspired by these elastohydrodynamic features, we exposed helical microswimmers to controlled shear flows in glass capillaries. Bending facilitated passage through highly curved microchannels. The deformation was elastic, and swimmers completely recovered their shape after passing through the corner under the externally applied flow with a rate of 2 ml/min (Fig. 3D). Increasing the stiffness of the filaments reduced deformation and led to obstruction of the channel (movie S5).

We conducted experiments in which the filaments were transported by a constant volume flux through a cylindrical channel with a constriction. Snapshots of experimental results are given in Fig. 3E. The passage through the constriction can be accommodated by a number of forces. Streamlines of the flow follow the conduit geometry; thus, the hydrodynamic drag forces exerted on a flexible filament produce a deformation that facilitates passage. These forces have components along the conduit axis and along a normal axis pointing inward, while both components promote passage. On the one hand, shear-induced elongation due to the difference in flow rates experienced by different parts of the body as it passes through the constriction decreases the radius of the helix, thus facilitating passage. On the other hand, the component of the hydrodynamic force pointing toward the conduit axis tends to compress the filament. This effect plays a more dominant role for helices going through sharp constrictions. The presence of the wall also modulates hydrodynamic forces acting on the filament. Lubrication stresses in the direction normal to the confining wall must be considered in the case of very narrow constrictions. To systematically explore the effect of shear-induced elongation, we built a numerical model by approximating the filament as a series of elastic segments of uniform helical shape (shown in the top panel of Fig. 3F). See section S5 for the details of the formulation. Snapshots of relevant experimental results and numerical simulations are given in Fig. 3 (E and F, respectively) (see movie S6). The simulations with slowly varying constriction were based on the experimental conditions and measured value of the Young's modulus (E = 9 kPa). The helix has three turns, a radius of 1.25 mm, a contour length of 33.3 mm, and a helix angle of 0.25π in its reference configuration.

As the helical filament entered the constriction, its axial length increased because of the higher flow rates experienced by parts of the helix closer to the constriction. This observation was faithfully captured in the simulation results. The plots of the speed of the two ends of the helix and the change in axial length are shown in fig. S6A. The front end speeds up as the filament enters the constriction, elongating the helix, and slows down as the filament exits the constriction, uniaxially compressing the helix. This leads to a deformed spiral shape of reduced local radius toward the side that was further in the constriction. The decrease

of radius accompanying the elongation enabled the helix to pass through the channel. Reduction in the flow rate generated a mirrored shape at the exit of the constriction, and the helix eventually regained its original shape (Fig. 3E). All these shape transformations were qualitatively captured by the simulations (Fig. 3F), which opens up the possibility to program the deformation of microswimmers for a given flow profile. Machines with a tubular body are less able to perform this accordion move, as the tubular body cannot be stretched by the shear stress. At flow rates higher than 5 ml/min, all tested machines passed through constrictions smaller than their diameter simply by getting compressed between the walls of the channel. Navigation based on squeezing comes with the risk of obstructing the channel, depending on the surface roughness and chemistry of the machines as well as the channel.

Autonomous shape-shifting driven by osmolarity

An appealing strategy to use different body plans for navigating in heterogeneous fluids engineers a shape transformation triggered by the microrheology of the fluid. Incorporation of stimulus-responsive materials opens the door to fabrication of microdevices that can react to changes in ambient temperature, pH, or osmolarity. Bacterial movement in search of environments with optimal water content is termed osmotaxis. Experiments performed with *E. coli* in polymer solutions revealed a long-term increase in swimming speed (41), which scale with the osmotic shock magnitude (42). Inspired by this mechanism, we tuned the mechanical and swelling properties of the nanocomposite by adding a hydrophilic comonomer and reducing the cross-linking degree (section S6 and movie S7). The increase in osmolarity dehydrates the swollen hydrogel and thereby reconfigures the body shape (fig. S7).

Our data suggest that a tubular body with a planar tail is preferable for swimming at low viscosity, while a helical morphology would perform better at high viscosity. We built a reconfigurable microswimmer programmed to undergo a shape transformation between these two configurations in response to an increase in sucrose concentration (Fig. 4A). While the motility gradually decreased with increasing viscosity, the step-out frequency increased because of reduction of body size. Step-out frequency denotes the maximum rotating speed at which the swimmers can still synchronize with the external rotating magnetic field. Reduction of body size provided two enhancements that led to higher step-out frequency, higher magnetization, and lower drag force. With the ability to increase the rotating frequency, the machines could be operated at a higher velocity. Therefore, the microswimmer with the programmed shape change exhibited a sustained velocity and enhanced maneuverability, despite the increase in viscous forces (Fig. 4B). To our knowledge, this is the first time that an artificial microswimmer increases its maximum rotating speed and maintains forward velocity with increasing viscosity. On the other hand, nonreconfigurable swimmers with the same initial configuration suffered from a significant drop in motility (Fig. 1F) and longer reorientation time (Fig. 2E) at higher viscosities. Different polymorphic forms are observed in nature under changing solvent conditions such as pH value, salinity, and temperature. To investigate the propulsion provided by reconfigurable helices, we developed two types of configurations that respond to changes in osmolarity by continuously coiling (type I) or uncoiling (type II), respectively (Fig. 4C and fig. S8). Type II helices sustained their motility, despite the changes in viscosity, while type I helices were slowed down by increasing drag (Fig. 4D). On the other hand, type I helices performed better when it came to navigation as expected.
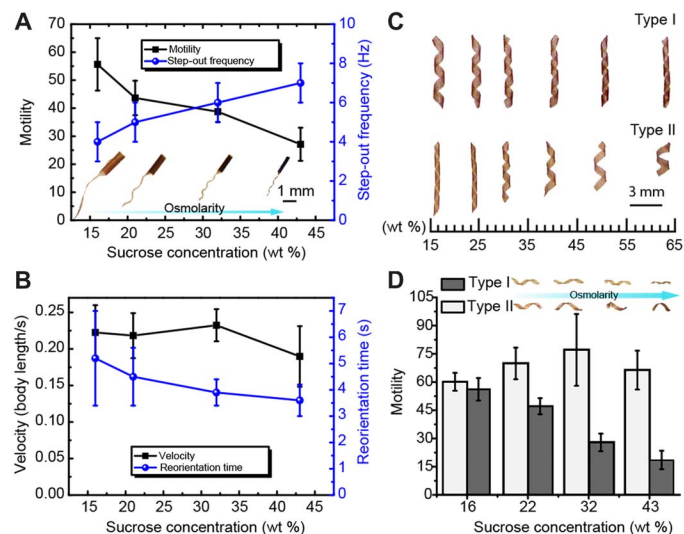
Fig. 4. Optimization of motility through shape-shifting driven by osmotic or shear stress. (**A**) Motility and step-out frequency of microswimmers in response to changes in sucrose concentration. The optical images show the effect of osmotic stress on the body and tail shapes. (**B**) Sustained velocity and enhanced maneuverability of microswimmers in response to changes in sucrose concentration. (**C**) Polymorphic transitions driven by osmolarity. Type I, continuously coiling with increasing osmolarity; type II, continuously uncoiling with increasing osmolarity. (**D**) The motility of the microswimmers can be kept constant by using polymorphic transitions to counteract viscous drag. All bar graphs represent average ± SEM ($n = 6$ measurements for each microswimmer and three different swimmers tested per condition).

CONCLUSION

In summary, we use magnetic hydrogel nanocomposites as a programmable matter to engineer microswimmers inspired by the form, locomotion, and plasticity of model microorganisms. We present methods for dynamic modulation of shapes, magnetization profiles, and locomotion gaits on the same device. A careful analysis of swimming performance at different viscosities provided a guideline to build a single machine that manifests multiple stable configurations, each optimized for a different locomotion gait. We perform shape adaptation in response to mechanical constraints and variation in osmotic pressure via the coordination between the elastic and viscous stresses. Our approach for solving the navigation problem reduces the number of elements to be controlled and therefore can have advantages in terms of speed, versatility, and cost. The manufacturing process is high throughput and scalable, which together open up doors for the development of a variety of adaptive soft microrobots.

METHODS
Materials
N-isopropylacrylamide (NIPAAm) as the monomer, acrylamide (AAm) as the hydrophilic comonomer, 2,2-dimethoxy-2-phenylacetophenone (99%) as the photoinitiator, and poly(ethylene glycol) diacrylate (PEGDA; average molecular weight, 575) as the cross-linker were all purchased from Sigma-Aldrich. MNPs (dispersible 1% polyvinylpyrrolidone-coated 30-nm magnetite) were obtained from Nanostructured & Amorphous Materials, Inc.

Fabrication of monolayer machines
Detailed fabrication processes of the monolayer structures can be found in our previous work (*27*). A PreGel nanocomposite solution

(NIPAAm/AAm/PEGDA and MNPs) was injected into a chamber constructed by sandwiching the glass mask and a silicon wafer with patterned SU-8 spacers. The SU-8 spacers define the thickness of the chamber, which is 30 μm. For the nonreconfigurable microswimmers, the molar ratio between NIPAAm/AAm/PEGDA was 100:0:5, and the concentration of MNPs was 5 weight % (wt %). Structures with smaller folding radius were obtained by increasing the MNP concentration to 10 wt %. After the PreGel solution filled the entire chamber, a gradient of MNPs was generated through gravitational sedimentation. Subsequently, a static uniform magnetic field with a strength of 10 mT and ultraviolet exposure (365 nm, 3 mW/cm^2) were simultaneously applied to the PreGel solution to align the MNPs while polymerizing the PreGel solution (fig. S2A). After curing, the sandwich construction was opened. The structures were released from the glass mask by submerging into water.

Experimental platform
The 3D alignment of the MNPs was performed using a solenoid in horizontal direction with an inner diameter of 14 cm in conjunction with a pair of Helmholtz coils separated by 5.5 inches in vertical direction (fig. S2A). Ultraviolet lamps (Lightning Enterprises, USA) were integrated inside the solenoid to initiate the cross-linking of hydrogel polymer. The maximum strength of generated uniform magnetic fields by the solenoid and Helmholtz coils are 10 and 5 mT at the center region, respectively. The motion studies were conducted with a custom-design eight-coil electromagnetic manipulation system (fig. S2C), which is called OctoMag (*43*). The maximum uniform magnetic field generated by the system is 40 mT, and the maximum magnetic field gradient is 1 T/m. We produced the confined channel used for hydrodynamic uncoiling experiments by connecting two glass pipettes using a glue gun. One of the open ends of the confined channel is connected to a syringe, as shown in fig. S2B. A syringe pump controls the flow rate. The viscosity of the sucrose solution was measured using the TA Instruments Rheometer AR 2000. Please see the Supplementary Materials for the details of characterization.

Preparation of osmolarity-responsive microswimmers
For the fabrication of type I reconfigurable microswimmers, a hydrophilic monomer AAm was incorporated into the gel solution with a molar ratio (NIPAAm/AAm/PEGDA) of 85:15:1. The molar ratio of type II is set as 100:0:1.

SUPPLEMENTARY MATERIALS
Supplementary material for this article is available at http://advances.sciencemag.org/cgi/content/full/5/1/eaau1532/DC1

Section S1. Programmable folding of monolayer nanocomposites
Section S2. Body size effect on flagellated microswimmers
Section S3. Characterization of the magnetization profile
Section S4. Analytical solution for an actuated elastic filament in a viscous fluid
Section S5. Elastic helical filament passing through a constriction
Section S6. Programmable shape transformation of monolayer structures
Fig. S1. Characterization of the folding mechanism of monolayer structures.
Fig. S2. Experimental platform.
Fig. S3. Effects of the machine body size on the precession.
Fig. S4. Characterization of the magnetic properties of the programmable nanocomposites using vibrating sample magnetometry measurements.
Fig. S5. Deformation of a flexible filament actuated from one end.
Fig. S6. Characterization of the elastic helix passing through the mechanical constraint.
Fig. S7. Characterization of the mechanical properties of hydrogel with various swelling properties.
Fig. S8. Coiling and uncoiling mechanism of self-folding monolayer structure.

Fig. S9. Measured viscosity of the media with varying concentration of sucrose.
Movie S1. Role of body plan on maneuverability.
Movie S2. Contribution of tail for stabilization during maneuvers.
Movie S3. Dynamically recording the magnetization profile.
Movie S4. Gait adaptation of tubular microswimmers with an elastic tail.
Movie S5. Shape adaptation in curved channels under axial flow with a rate of 2 ml/min.
Movie S6. Shape transformation in a constriction under an axial flow with a rate of 5 ml/min.
Movie S7. Polymorphism of helix programmed by tuning the material composition.
References (44–47)

REFERENCES AND NOTES

1. K. F. Jarrell, M. J. McBride, The surprisingly diverse ways that prokaryotes move. *Nat. Rev. Microbiol.* **6**, 466–476 (2008).
2. E. M. Purcell, Life at low Reynolds number. *Am. J. Phys.* **45**, 3–11 (1977).
3. E. Lauga, Bacterial hydrodynamics. *Annu. Rev. Fluid Mech.* **48**, 105–130 (2016).
4. K. D. Young, The selective value of bacterial shape. *Microbiol. Mol. Biol. Rev.* **70**, 660–703 (2006).
5. G. Langousis, K. L. Hill, Motility and more: The flagellum of Trypanosoma brucei. *Nat. Rev. Microbiol.* **12**, 505–518 (2014).
6. S. S. Justice, D. A. Hunstad, L. Cegelski, S. J. Hultgren, Morphological plasticity as a bacterial survival strategy. *Nat. Rev. Microbiol.* **6**, 162–168 (2008).
7. B. Liu, M. Gulino, M. Morse, J. X. Tang, T. R. Powers, K. S. Breuer, Helical motion of the cell body enhances *Caulobacter crescentus* motility. *Proc. Natl. Acad. Sci. U.S.A.* **111**, 11252–11256 (2014).
8. K. Son, F. Menolascina, R. Stocker, Speed-dependent chemotactic precision in marine bacteria. *Proc. Natl. Acad. Sci. U.S.A.* **113**, 8624–8629 (2016).
9. M. J. Kühn, F. K. Schmidt, B. Eckhardt, K. M. Thormann, Bacteria exploit a polymorphic instability of the flagellar filament to escape from traps. *Proc. Natl. Acad. Sci. U.S.A.* **114**, 6340–6345 (2017).
10. M. Sitti, H. Ceylan, W. Hu, J. Giltinan, M. Turan, S. Yim, E. Diller, Biomedical applications of untethered mobile milli/microrobots. *Proc. IEEE* **103**, 205–224 (2015).
11. J. Li, B. Esteban-Fernández de Ávila, W. Gao, L. Zhang, J. Wang, Micro/nanorobots for biomedicine: Delivery, surgery, sensing, and detoxification. *Sci. Robot.* **2**, eaam6431 (2017).
12. B. J. Nelson, I. K. Kaliakatsos, J. J. Abbott, Microrobots for minimally invasive medicine. *Annu. Rev. Biomed. Eng.* **12**, 55–85 (2010).
13. W. Hu, G. Z. Lum, M. Mastrangeli, M. Sitti, Small-scale soft-bodied robot with multimodal locomotion. *Nature* **554**, 81–85 (2018).
14. L. Zhang, J. J. Abbott, L. Dong, B. E. Kratochvil, D. Bell, B. J. Nelson, Artificial bacterial flagella: Fabrication and magnetic control. *Appl. Phys. Lett.* **94**, 064107 (2009).
15. A. Ghosh, P. Fischer, Controlled propulsion of artificial magnetic nanostructured propellers. *Nano Lett.* **9**, 2243–2245 (2009).
16. R. Dreyfus, J. Baudry, M. L. Roper, M. Fermigier, H. A. Stone, J. Bibette, Microscopic artificial swimmers. *Nature* **437**, 862–865 (2005).
17. L. Ricotti, B. Trimmer, A. W. Feinberg, R. Raman, K. K. Parker, R. Bashir, M. Sitti, S. Martel, P. Dario, A. Menciassi, Biohybrid actuators for robotics: A review of devices actuated by living cells. *Sci. Robot.* **2**, eaaq0495 (2017).
18. C. Cvetkovic, R. Raman, V. Chan, B. J. Williams, M. Tolish, P. Bajaj, M. S. Sakar, H. H. Asada, M. Taher, A. Saif, R. Bashir, Three-dimensionally printed biological machines powered by skeletal muscle. *Proc. Natl. Acad. Sci. U.S.A.* **111**, 10125–10130 (2014).
19. S.-J. Park, M. Gazzola, K. S. Park, S. Park, V. Di Santo, E. L. Blevins, J. U. Lind, P. H. Campbell, S. Dauth, A. K. Capulli, F. S. Pasqualini, S. Ahn, A. Cho, H. Yuan, B. M. Maoz, R. Vijaykumar, J.-W. Choi, K. Deisseroth, G. V. Lauder, L. Mahadevan, K. K. Parker, Phototactic guidance of a tissue-engineered soft-robotic ray. *Science* **353**, 158–162 (2016).
20. B. J. Williams, S. V. Anand, J. Rajagopalan, M. T. A. Saif, A self-propelled biohybrid swimmer at low Reynolds number. *Nat. Commun.* **5**, 3081 (2014).
21. J. Rogers, Y. Huang, O. G. Schmidt, D. H. Gracias, Origami MEMS and NEMS. *MRS Bull.* **41**, 123–129 (2016).
22. K. Malachowski, M. Jamal, Q. Jin, B. Polat, C. J. Morris, D. H. Gracias, Self-folding single cell grippers. *Nano Lett.* **14**, 4164–4170 (2014).
23. J. Na, A. A. Evans, J. Bae, M. C. Chiappelli, C. D. Santangelo, R. J. Lang, T. C. Hull, R. C. Hayward, Programming reversibly self-folding origami with micropatterned photo-crosslinkable polymer trilayers. *Adv. Mater.* **27**, 79–85 (2015).
24. M. Z. Miskin, K. J. Dorsey, B. Bircan, Y. Han, D. A. Muller, P. L. McEuen, I. Cohen, Graphene-based bimorphs for micron-sized, autonomous origami machines. *Proc. Natl. Acad. Sci. U.S.A.* 466–470 (2018).
25. Y. Klein, E. Efrati, E. Sharon, Shaping of elastic sheets by prescription of non-euclidean metrics. *Science* **315**, 1116–1120 (2007).
26. J. Kim, J. A. Hanna, M. Byun, C. D. Santangelo, R. C. Hayward, Designing responsive buckled surfaces by halftone gel lithography. *Science* **335**, 1201–1205 (2012).
27. H.-W. Huang, M. S. Sakar, A. J. Petruska, S. Pané, B. J. Nelson, Soft micromachines with programmable motility and morphology. *Nat. Commun.* **7**, 12263 (2016).
28. H. C. Berg, R. A. Anderson, Bacteria swim by rotating their flagellar filaments. *Nature* **245**, 380–382 (1973).
29. H.-W. Huang, T.-Y. Huang, M. Charilaou, S. Lyttle, Q. Zhang, S. Pané, B. J. Nelson, Investigation of magnetotaxis of reconfigurable micro-origami swimmers with competitive and cooperative anisotropy. *Adv. Funct. Mater.* **28**, 1802110 (2018).
30. E. J. Smith, D. Makarov, S. Sanchez, V. M. Fomin, O. G. Schmidt, Magnetic microhelix coil structures. *Phys. Rev. Lett.* **107**, 097204 (2011).
31. T. M. Bartlett, B. P. Bratton, A. Duvshani, A. Miguel, Y. Sheng, N. R. Martin, J. P. Nguyen, A. Persat, S. M. Desmarais, M. S. VanNieuwenhze, K. C. Huang, J. Zhu, J. W. Shaevitz, Z. Gitai, A periplasmic polymer curves *Vibrio cholerae* and promotes pathogenesis. *Cell* **168**, 172–185.e15 (2017).
32. H.-W. Huang, Q. Chao, M. S. Sakar, B. J. Nelson, Optimization of tail geometry for the propulsion of soft microrobots. *IEEE Robot. Autom. Lett.* **2**, 727–732 (2017).
33. O. S. Pak, W. Gao, J. Wang, E. Lauga, High-speed propulsion of flexible nanowire motors: Theory and experiments. *Soft Matter* **7**, 8169–8181 (2011).
34. M. A. Constantino, M. Jabbarzadeh, H. C. Fu, R. Bansil, Helical and rod-shaped bacteria swim in helical trajectories with little additional propulsion from helical shape. *Sci. Adv.* **2**, e1601661 (2016).
35. B. Ni, B. Ghosh, F. S. Paldy, R. Colin, T. Heimerl, V. Sourjik, Evolutionary remodeling of bacterial motility checkpoint control. *Cell Rep.* **18**, 866–877 (2017).
36. Ò. Guadayol, K. L. Thornton, S. Humphries, Cell morphology governs directional control in swimming bacteria. *Sci. Rep.* **7**, 2061 (2017).
37. K. Son, J. S. Guasto, R. Stocker, Bacteria can exploit a flagellar buckling instability to change direction. *Nat. Phys.* **9**, 494–498 (2013).
38. Marcos, H. C. Fu, T. R. Powers, R. Stocker, Bacterial rheotaxis. *Proc. Natl. Acad. Sci. U.S.A.* **109**, 4780–4785 (2012).
39. A. Persat, C. D. Nadell, M. K. Kim, F. Ingremeau, A. Siryaporn, K. Drescher, N. S. Wingreen, B. L. Bassler, Z. Gitai, H. A. Stone, The mechanical world of bacteria. *Cell* **161**, 988–997 (2015).
40. H. Noguchi, G. Gompper, Shape transitions of fluid vesicles and red blood cells in capillary flows. *Proc. Natl. Acad. Sci. U.S.A.* **102**, 14159–14164 (2005).
41. V. A. Martinez, J. Schwarz-Linek, M. Reufer, L. G. Wilson, A. N. Morozov, W. C. K. Poon, Flagellated bacterial motility in polymer solutions. *Proc. Natl. Acad. Sci. U.S.A.* **111**, 17771–17776 (2014).
42. J. Rosko, V. A. Martinez, W. C. K. Poon, T. Pilizota, Osmotaxis in *Escherichia coli* through changes in motor speed. *Proc. Natl. Acad. Sci. U.S.A.* **114**, E7969–E7976 (2017).
43. M. P. Kummer, J. J. Abbott, B. E. Kratochvil, R. Borer, A. Sengul, B. J. Nelson, OctoMag: An electromagnetic system for 5-DOF wireless micromanipulation. *IEEE Trans. Robot.* **26**, 1006–1017 (2010).
44. S. Champmartin, A. Ambari, N. Roussel, Flow around a confined rotating cylinder at small Reynolds number. *Phys. Fluids* **19**, 103101 (2007).
45. T. S. Yu, E. Lauga, A. E. Hosoi, Experimental investigations of elastic tail propulsion at low Reynolds number. *Phys. Fluids* **18**, 2–6 (2006).
46. E. Lauga, W. R. DiLuzio, G. M. Whitesides, H. A. Stone, Swimming in circles: Motion of bacteria near solid boundaries. *Biophys. J.* **90**, 400–412 (2006).
47. N. C. Darnton, H. C. Berg, Force-extension measurements on bacterial flagella: Triggering polymorphic transformations. *Biophys. J.* **92**, 2230–2236 (2007).